Cross-section measurements of neutron-deuteron breakup at 13.0 MeV

H. R. Setze,* C. R. Howell, W. Tornow, R. T. Braun, D. E. González Trotter, A. H. Hussein,†
R. S. Pedroni,‡ C. D. Roper, F. Salinas, I. Šlaus,¶ B. Vlahović,§ and R. L. Walter
Duke University and Triangle Universities Nuclear Laboratory, Durham, North Carolina 27708, USA

G. Mertens
Institute of Physics, University of Tübingen, D-72074 Tübingen, Germany

J. M. Lambert
Department of Physics, Georgetown University, Washington, District of Columbia 20057, USA

H. Witała
Institute of Physics, Jagellonian University, Reymonta 4, PL-30059 Cracow, Poland

W. Glöckle
Institut für Theoretishe Physik II, Ruhr-Universität Bochum, D-44780 Bochum, Germany
(Received 16 August 2004; published 23 March 2005)

Cross-section measurements of seven exit-channel configurations in the neutron-deuteron breakup at 13.0 MeV are reported and compared to rigorous calculations. Our data are consistent with those of previous measurements in four of six configurations. The present data for five configurations are in good agreement with theoretical predictions. The cross-section data for the space-star and another out-of-plane configuration are larger than the theoretical predictions by more than three standard deviations. The previously observed 20% discrepancy between theory and data for the space-star configuration is confirmed in the present work. The inclusion of the Tucson-Melbourne 2π-exchange three-nucleon force changes the predicted cross section by only 2% and in the wrong direction needed to bring theory into agreement with data.

DOI: 10.1103/PhysRevC.71.034006 PACS number(s): 25.10.+s, 25.40.Dn, 21.30.−x

I. INTRODUCTION

It is well established that few-nucleon forces must exist at some level in any model of nuclear systems with $A > 2$, if the model is based on two-nucleon ($2N$) interactions in which nucleons are treated as constituent particles without internal structure [1]. Searches for experimental evidence of three-nucleon ($3N$) forces have been conducted for more than 30 years, but they have not provided conclusive results. The strongest evidence to date for a three-nucleon force (3NF) effect is the triton binding-energy anomaly. Calculations of the triton binding energy using realistic $2N$ force models are about 1 MeV lower than the experimental value of 8.5 MeV [2,3]. This discrepancy between data and calculations has inspired most 3NF models [4–7]. Because the bound state covers a very limited region of $3N$ phase space, the remedy of the triton binding problem by the addition of a 3NF only gives a minimum test of the applied 3NF model. The full development of 3NF models demand guidance obtained from comparisons to both bound-state and continuum data.

The difficulty in obtaining definitive evidence of 3NF effects in the $3N$ continuum is understandable since such effects are always shadowed by the dominant $2N$ forces and require sophisticated theoretical analyses of the experimental observables. In the past, discrepancies between $3N$ data and calculations were usually attributed to inadequacies in the $3N$ calculations and the $2N$ force models used. Now, exact numerical solutions of $3N$ Faddeev equations for the continuum are available with $2N$ forces only [8] and with $2N$ plus $3N$ forces [9,10]. Also, a variety of realistic $2N$ force models are available [11–19]. Very promising is the appearance of the new generation of high-precision NN potentials [16–19], which fit exactly the existing NN data basis with χ^2 per data point close to 1.

The availability of these new high-accuracy $3N$ calculations and the realistic $2N$ potentials opens new avenues for exploring 3NF effects. One possible direction is to obtain a collection of $3N$ continuum observables that cannot be adequately described using only $2N$ forces. Such an assembly of data would provide the long-needed database for developing realistic 3NF models that are adjusted to fit bound-state properties and continuum observables. A number of cases reporting large discrepancies between nucleon-deuteron (N-d) data and calculations using only $2N$ forces appear in the literature [10,20–41], but more are needed. In the case of elastic scattering, the discrepancies for the cross sections and some polarization observables have

*Present address: Pearl River Community College, Poplarville, MS 39470, USA.
†Present address: Physics Department, Univ. of Northern British Columbia, Prince George, BC, Canada.
‡Present address: Physics Department, North Carolina A&T State Univ., Greensboro, NC 27411, USA.
¶Permanent address: Rudjer Boskovic Institute, Zagreb, Croatia.
§Present address: Physics Department, North Carolina Central Univ., Durham, NC 27707, USA.

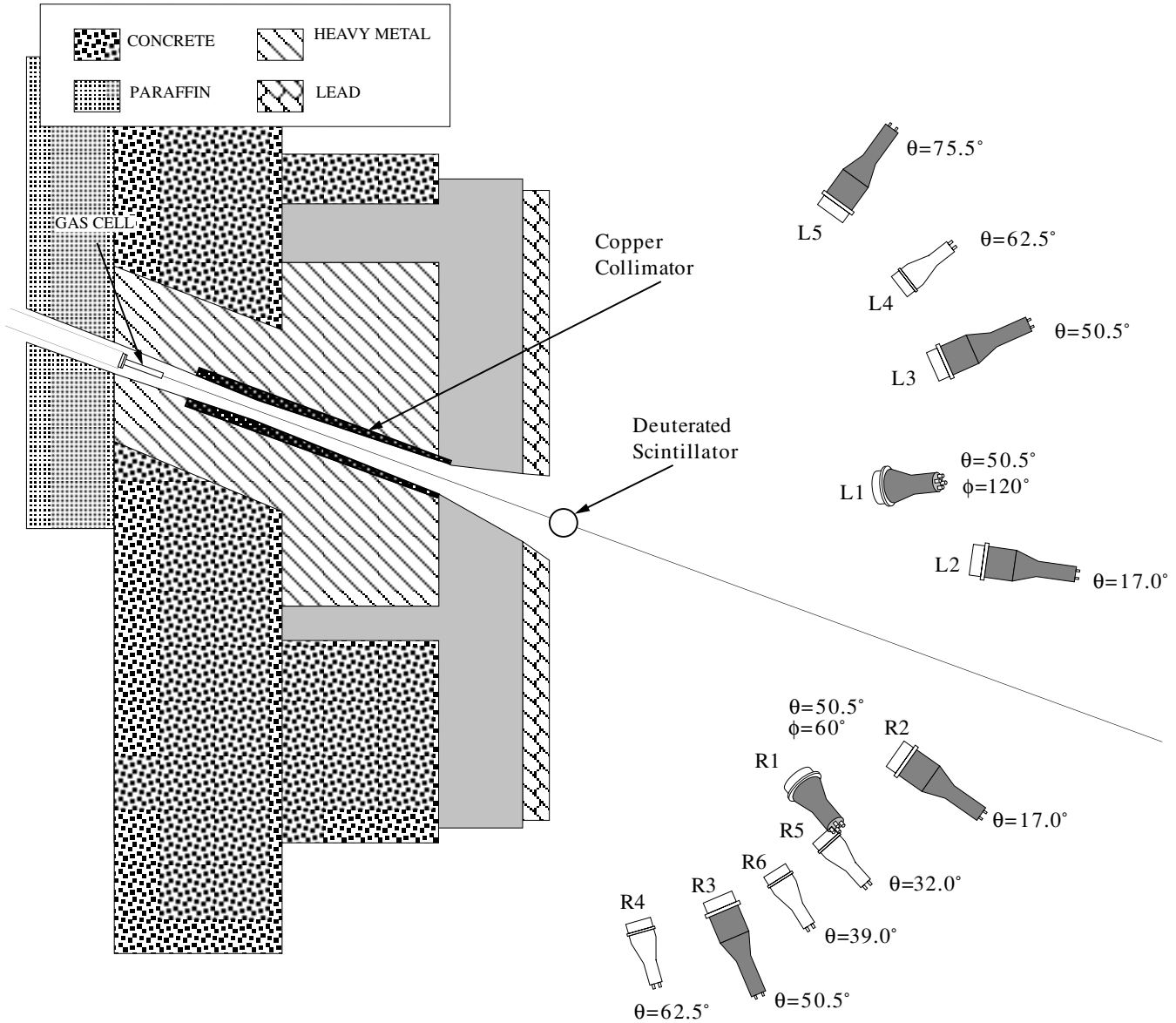

FIG. 1. Schematic of experimental setup for ^{2}H(*n*,*nnp*) cross-section measurements.

been found at higher energies. These discrepancies, to a large extent, can be removed by present-day 3NF models [42–46].

The present work was motivated by the results of Strate *et al*. [21]. Rigorous 3*N* calculations are about 25% lower than their cross-section data for the space-star and coplanar-star configurations, in neutron-deuteron (*nd*) breakup at 13.0 MeV. In the star configuration, the momentum vectors of the three emitted nucleons in the c.m. lie in the same plane, have equal magnitude, and are separated by 120°. The plane defined by the momentum vectors can be oriented arbitrarily in space. The space and coplanar stars are two extreme orientations of the plane. In the space star, the plane is perpendicular to the incident beam axis; in the coplanar star, the incident beam momentum vector lies in the star plane. The relative discrepancies between rigorous *nd* calculations and the data of Strate *et al*. [21] for the star configurations are the largest ever reported for a *nd* cross section. Because of the implications that their findings might be the long-sought signature for 3NF effects in the continuum, we felt it important to verify their findings. Our first results were reported by Setze *et al*. [31]. In this paper, we report our cross-section data for seven exit-channel configurations in *nd* breakup at 13.0 MeV. Details of the experimental techniques and analysis methods used in the present work and in [31] are given here. Our data are compared to the data of Strate *et al*. [21], to the proton-deuteron (*pd*) data of Rauprich *et al*. [30], and to rigorous *nd* calculations made with and without 3NF.

II. EXPERIMENTAL DETAILS

Measurements were performed using a shielded neutron source at the Triangle Universities Nuclear Laboratory (TUNL). The experimental setup is shown in Fig. 1. The scatterer was a $C_6{}^2H_{12}$ liquid deuterated scintillator (DS). The

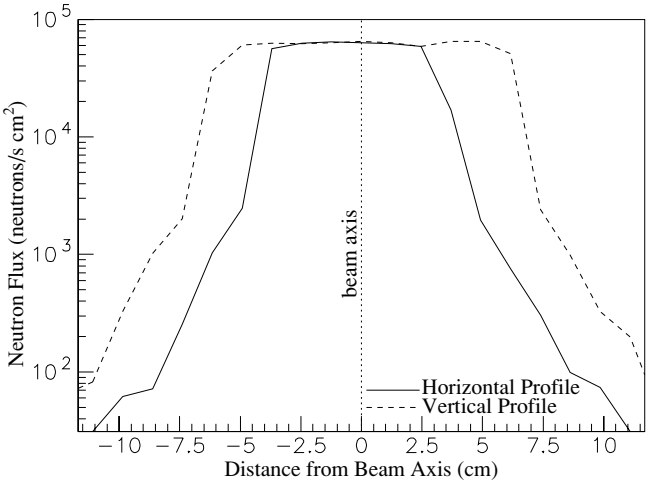

FIG. 2. Neutron beam profile of the collimated source used in the ^{2}H(*n*,*nnp*) cross-section measurements. The profile was taken at the location of the deuteron scatterer with 13.0-MeV neutrons.

scintillator fluid (NE-232) was encapsulated in a glass cylinder with outer dimensions of 4.2 cm in diameter and 6.4 cm high and with a wall thickness of 2 mm. The DS was bombarded with a dc beam of 13.0-MeV neutrons produced using the ^{2}H(*d*,*n*) reaction. The neutron production target was a 3-cm-long cell pressurized to 7.8 atm. The deuteron beam current maintained on the cell was 1.5 μA. The beam entrance window on the production cell was a 6.35-μm-thick Havar foil. A 0.5-mm-thick gold disk capped the end of the cell and was used to stop the deuteron beam. The cell was water cooled and electrically isolated from the rest of the beam line. The charge deposited by the beam on the cell was measured using a beam-current integration circuit. The energy spread in the neutron beam was $\pm$0.19 MeV and was mainly due to the energy loss of the incident deuteron beam in the deuterium gas.

The center-to-center distance between the neutron production cell and the DS was 1.7 m. The collimator in the shielding wall was designed such that the DS was illuminated uniformly by unscattered neutrons. The neutron beam profile at the location of the DS is shown in Fig. 2. The flux was constant across the surface of the DS and dropped by a factor of 10^3 at a distance of 10 cm from the incident neutron beam axis. The charge deposited on the beam stop was measured, and the direct neutron flux was monitored with a detector positioned on the beam axis about 4 m downstream from the DS. The monitor detector was a rectangular liquid scintillator with dimensions 4.5 $\times$ 15.8 $\times$ 7.6 cm.

The integrated beam-target luminosity $\mathcal{L}$, which is the product of the DS thickness and total number of neutrons incident on the DS, was determined by measuring the yields for *nd* elastic scattering. The simultaneous accumulation of the breakup and elastic-scattering data reduced the sensitivity of the measurements to system dead times and absolute detection efficiencies. The kinematics for both event types—breakup and elastic scattering—were experimentally overdetermined. The redundancy in the measurement of kinematic quantities was used to reduce backgrounds. For the breakup events, the momentum of each neutron and the energy of the proton were measured. For the elastic-scattering events, the momentum of the scattered neutron and the energy of the recoil deuteron were measured. The neutrons were detected by an array of 11 liquid scintillators with pulse-shape discrimination, and the protons from the breakup reaction and the recoil deuterons from elastic scattering were detected in the DS. The positions and characteristics of the neutron detectors are given in Table I. Eight of the 11 neutron detectors were positioned at angles symmetric about the beam axis, facilitating the investigation of systematic errors and increasing the counting rate for some *nd* breakup configurations.

Data were stored for two event trigger-types: double (DS and one neutron detector) and triple (DS and two neutron detectors) coincidences. The trigger signals were generated in a two-staged coincidence circuit using the timing signal from each neutron detector and the DS. The DS threshold was set to detect deuterons with energies down to 100 keV. The neutron-detector thresholds ranged from a neutron energy of 0.40 MeV for the most backward-angle detectors to 0.75 MeV for the forward-angle detectors. With these thresholds, the counting rate in each neutron detector was about 4 kHz and that in the DS was 500 kHz. In the first stage of the coincidence circuit, double-coincidence signals were formed between the DS and each neutron detector. The width of the coincidence

TABLE I. Neutron-detector positions and attributes. All detectors were cylindrical in shape and 5.08 cm thick.

Detector	θ	ϕ	Flight path (cm)	Diameter (cm)	Fluid type
R1	50.5°	60°	149.8	12.7	BC 501
R2	17.0°	0°	152.2	12.7	BC 501
R3	50.5°	0°	151.8	12.7	BC 501
R4	62.5°	0°	153.2	11.4	NE 213
R5	32.0°	0°	154.0	11.4	NE 213
R6	39.0°	0°	151.6	11.4	NE 213
L1	50.5°	120°	149.9	12.7	BC 501
L2	17.0°	180°	152.9	12.7	BC 501
L3	50.5°	180°	154.2	12.7	BC 501
L4	62.5°	180°	176.9	11.4	NE 213
L5	75.5°	180°	162.9	12.7	BC 501

window was 280 ns, and the relative timing and widths of the signals at the double-coincidence circuit were set so that the timing of the coincidence signal was defined by the DS timing signal. The prescaled double-coincidence signals provided the triggers for collecting the events for *nd* elastic scattering. The prescale factor was set to 100 to keep the data-acquisition dead time less than 5%. The trigger signals for the breakup events were generated in the second stage of the circuit by forming a coincidence between any two of the six double-coincidence signals within a resolving time of 540 ns.

The following parameters were recorded on tape for each event-trigger: the hit pattern in the neutron-detector array, the particle time of flight (TOF) between the DS and each neutron detector, the light output of the DS and of each neutron detector, and the pulse-shape time of each neutron detector. The aggregate (breakup plus prescaled elastic scattering) trigger rate was 120 Hz, and the rates of the two trigger types were about equal. The dead time of the data-acquisition (DAQ) system was about 3%. The detector-dependent dead times of our system, which were always less than 3%, were measured by flashing the scintillators with light pulses through fiberoptic cables.

III. DATA ANALYSIS

In this section we describe the analyses of the elastic-scattering and breakup data. The time-integrated beam-target luminosity $\mathcal{L}$ and the light response function of the DS were obtained from the elastic-scattering data.

A. Monte Carlo simulations

Both analyses depended heavily on accurate computer simulations of the experiment to account for finite geometry, beam-energy spreads, and detector time and energy resolutions. The simulations contained the finite geometry of our experimental setup and included the time and energy resolution of detectors and the multiple scattering (in- and out-scattering) of neutrons in the DS and air. The forced-scattering method was employed for efficiency wherein each incident deuteron on the neutron production cell produced a neutron that interacted in the DS. The reaction was either *nd* elastic scattering into the angular acceptance of a particular detector or *nd* breakup with the neutrons emitted in the direction of two chosen detectors. The flow of each simulated event followed the direction of the physical process in the experiment. Each event was started by choosing three points at randomly picked locations in the deuteron gas cell, inside the DS, and inside the neutron detector. For breakup events, a fourth point was chosen inside the second neutron detector. The 400-keV spread in the energy of the incident neutron beam, which was primarily due to the energy loss of the deuteron beam in the deuterium gas of the production target, was modeled in the simulation with a linear function. The energies of the produced neutrons varied linearly from the minimum to the maximum value as a function of the position in the cell where the neutron was produced. The neutron was transported to the interaction point in the DS without attenuation. Attenuation (out-scattering) was not recorded in this segment because it was identical for elastic and breakup events. From this point, the details of tracking the neutrons in elastic scattering and in the breakup reaction were different and will be discussed separately.

For elastic-scattering events, a random number was generated to determine whether the neutron scattered once more before heading toward the detector. Several parameters were recorded for each simulated event: the pulse height in the DS, the neutron TOF, the neutron detection efficiency, the neutron transmission in transport to the front of the neutron detector, and a probability weighting factor that accounted for the energy spread in the DS and the cross section of the process. The deuteron energy was converted to pulse height using the measured light response function of the DS and smeared over the pulse-height resolution of the DS using a skewed Gaussian function. The neutron TOF was computed from the neutron energy and dispersed over a Gaussian distribution with a width equal to the net time resolution [2.4 ns full width at half maximum (FWHM)] of the DS and neutron detector. The probability weighting factor was calculated as the product of the cross section and the value of the normalized Gaussian function used to distribute the DS pulse heights. The neutron detection efficiencies used in the simulations were measured in a separate experiment, and the transmissions were calculated using the neutron total cross sections for the materials that the neutrons traversed in their flight from the interaction point in the DS to the front of the neutron detector. The differential cross sections used in the library for the simulations were from rigorous three-nucleon calculations.

B. Analysis of elastic-scattering data

The elastic-scattering data were obtained from the analysis of the double-coincidence events. The two primary histograms used in these analyses were of the neutron TOF and the DS pulse height. The elastic-scattering data were analyzed with the same detector thresholds used in the breakup analysis.

Two DS pulse-height (DSPH) spectra were accumulated, one containing true- and accidental-coincidence events (referred to as *true+accidental* events) and the other containing only accidental coincidences (referred to as *accidental* events). A TOF spectrum for *nd* elastic scattering to one of the neutron detectors is shown in Fig. 3. Two gates were set in each neutron TOF histogram, and an associated DSPH histogram was accumulated for events with neutron TOF values within each gate. One gate was set around the elastic-scattering peak and the other was set with equal width in the region corresponding to flight times less than that of the prompt γ rays. The second gate was used to determine the accidental-coincidence background underneath the elastic-scattering peak in the DSPH spectrum. The two DSPH histograms for elastic scattering to 50.5° are overlaid in Fig. 4(a). Notice that the accidental-coincidence background does not account for all the counts to the left of the elastic-scattering peak. The Monte Carlo simulations (MC) account for the remaining background as being mainly due to neutron in-scattering; see Fig. 4(b). The measured DSPH spectrum after subtraction of accidental-coincidence and in-scattering backgrounds is shown in Fig. 4(c).

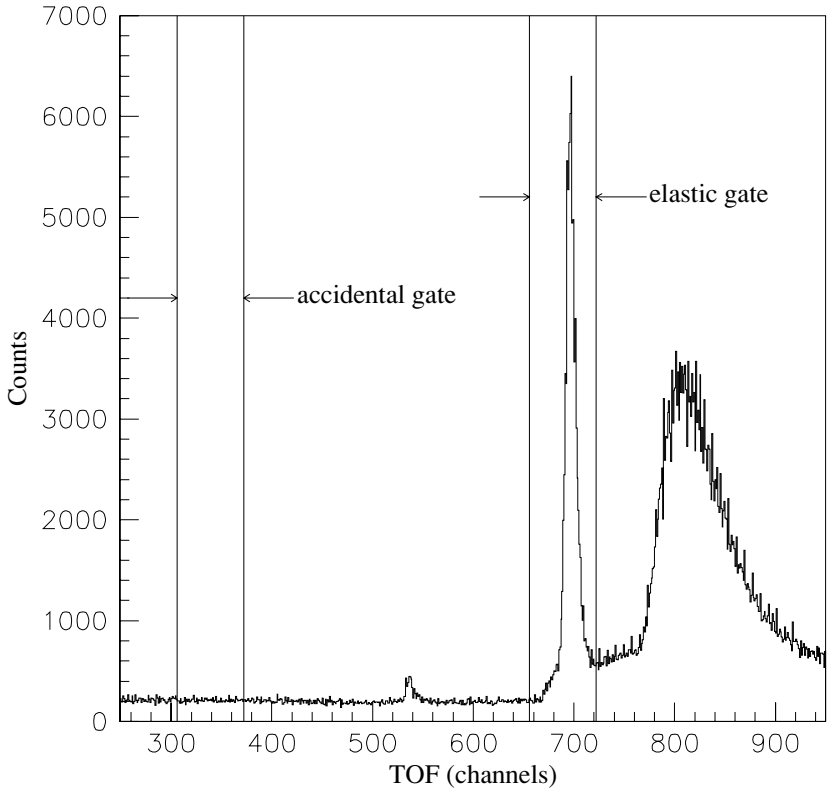

FIG. 3. TOF spectrum for double-coincidence events. Time increases from left to right, and the time calibration is 0.2 ns/channel. The small peak between the gates is due to prompt γ rays that leak through the pulse-shape-discrimination (PSD) cut. The large mound to the right of the elastic peak is the continuum of neutrons from *nd* breakup and *nd* elastic scattering of continuum neutrons from breakup reactions in the gas cell.

1. Determination of the luminosity

Any mechanism that can cause a loss or gain in the yields in the DSPH histogram directly impacts our determination of $\mathcal{L}$. Two mechanisms that can cause a loss of elastic-scattering yields are accidental triple coincidences and edge effects of the deuterated scintillator. Our data were corrected for both processes.

To make the trigger types mutually exclusive, double-coincidence triggers were suppressed in hardware by the occurrence of a triple coincidence. A consequence of this logic is that some elastic-scattering events were lost from the double-coincidence trigger to the triple-coincidence trigger because of accidental triple coincidences. The loss of elastic-scattering events from the double-coincidence spectra occurred whenever an elastically scattered neutron was detected and an uncorrelated event occurred in any of the other detectors within the triple-coincidence time window. The loss in the elastic-scattering yields for each detector due to this type of accidental-triple coincidence was about 1%. Because the accidental-coincidence rate between any two detectors depends on the counting rate in each detector, the percentage of elastic yields lost due to the accidental triple coincidences was slightly detector dependent.

If a neutron scatters from a deuteron near the edge of the DS, the recoiling deuteron may hit the scintillator wall before depositing all its energy. As the scattering angle of the neutron increases, the recoil energy of the deuteron also increases, which in turn increases the range of the deuteron in the scintillator fluid. Consequently, the fraction of recoil deuterons that have some undetected energy increases with increasing scattering angle. This effect was calculated in the MC simulation. The correction was less than 3%.

In our analysis, we accounted for neutron attenuation, neutron in-scattering effects, and finite-geometry effects. To correct the data for these effects, the entire experiment was simulated as described above. Our treatment and the size of each effect in our measurements are discussed below.

The neutron attenuation is primarily caused by neutron interactions in the fluid and containment vessel of the DS. Other materials that attenuate the neutrons are the DS light shield and the air between the DS and the neutron detectors. The neutron transmission was computed in the MC simulation using total cross sections of the carbon and deuterium neutrons. The average transmission of the neutrons from the interaction points inside the DS to the neutron detector was about 0.78. The relative uncertainty in the calculated transmission is $\pm 1.3\%$ and is mostly due to the uncertainties in the carbon and deuterium neutron total cross sections, which have reported uncertainties less than $\pm 1\%$.

The in-scattering contributions to the double-coincidence spectra were also computed in the MC simulations. Because triple scattering is expected to contribute less than 1% of the *nd* elastic-scattering yields, only single- and double-scattering were included in the simulations. The processes considered were neutron elastic scattering from deuterium and elastic and inelastic scattering of neutrons from carbon. As shown in Fig. 4(b), between 5 and 10% of the detected yield for elastic scattering was due to in-scattered neutrons in the DS. We estimate the uncertainty in our in-scattering simulation to be about $\pm 5\%$ of the effect. This uncertainty is mainly due

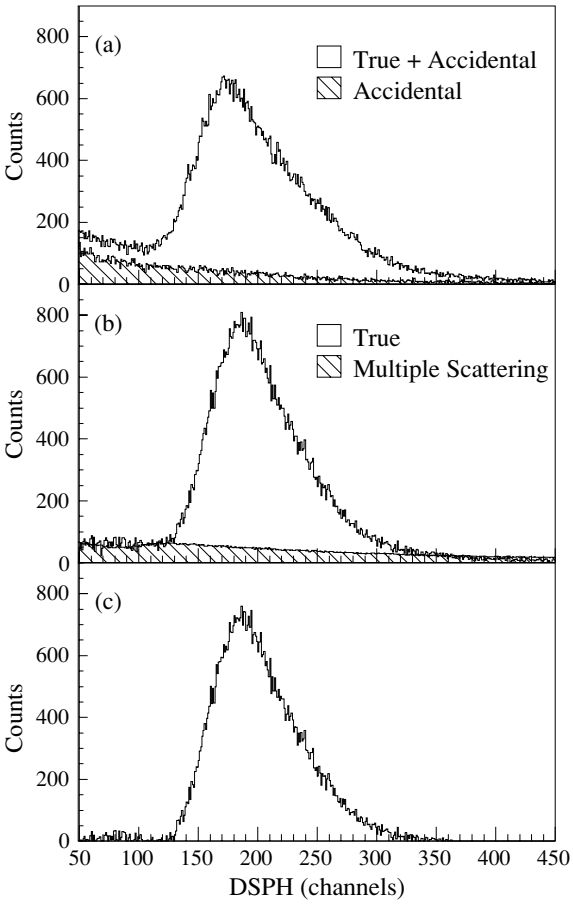

FIG. 4. Histograms of the deuterated-scintillator pulse height for *nd* elastic scattering at 50.5°. (a) The DSPH histograms for true + accidental and accidental events. (b) The DSPH spectrum after subtraction of counts due to accidental events. The contribution from multiple scattering was calculated in the MC simulation. (c) The final spectrum contains only singly-scattered events after subtraction of counts due to accidental and multiple-scattering events.

to the reported errors on the differential cross-section data for neutron scattering from carbon and deuterium.

The finite-geometry effects were sizable in our measurements because of the large DS and neutron detectors and the short flight paths needed to obtain practical triple-coincidence counting rates. For example, the angular spreads in the space-star configuration were $\pm 4.0^\circ$ in the polar scattering angle θ and $\pm 7.2^\circ$ in the azimuthal scattering angle ϕ. The angular acceptance and the spread in the incident beam energy caused the data to be distributed about the point-geometry kinematic parameters. These effects were included in the simulations of the elastic-scattering and breakup events.

The value of $\mathcal{L}$ is related to the elastic-scattering yields by

$$Y_{\rm el}(\theta) = \left\langle \frac{d\sigma}{d\Omega}(\theta) \right\rangle_{\rm lab} d\Omega\, \bar{\alpha}(E_{\rm el})\, \bar{\epsilon}(E_{\rm el})\, \mathcal{L}. \qquad (3.1)$$

The $Y_{\rm el}$ is the net elastic-scattering yields, the $\langle d\sigma/d\Omega \rangle$ is the acceptance- and energy-averaged differential cross section for *nd* elastic scattering in the laboratory system, θ is the mean laboratory scattering angle, $d\Omega$ is the detector solid angle, $\bar{\alpha}$ is the acceptance- and energy-averaged neutron transmission from the DS to the neutron detector, $\bar{\epsilon}$ is the energy-averaged efficiency of the neutron detector around the energy of the elastically scattered neutrons. The quantities $\bar{\alpha}$, $\bar{\epsilon}$, and $\langle d\sigma/d\Omega \rangle$ were computed in the simulations. The net yields (background subtracted, corrected for in-scattering and accidental triple coincidences) were extracted from the DSPH spectra.

A value for $\mathcal{L}$ was determined from the elastic-scattering yields measured in each of nine detectors, i.e., all but the two detectors at 17°. Since the deuteron recoil energy for neutrons scattering to 17° was below our lower-level threshold setting on the DS, the elastic-scattering yields from the detectors at 17° were excluded in the analysis. Because the measured $\mathcal{L}$ should be the same for all detectors, the deviation of the values from the average value was assigned to be the systematic error in $\mathcal{L}$. The uncertainty in our determination of the luminosity was $\pm 3.5\%$ and dominated by the systematic uncertainties, which were mostly due to our extraction of the *nd* elastic-scattering yields and uncertainties in the absolute neutron detection efficiency.

The systematic uncertainty in the elastic-scattering yield was mainly caused by uncertainties in our description of the background ($<3\%$) that remained in the DSPH histograms after subtraction of the accidental coincidences and multiple scattering. These backgrounds were believed to be due to neutron multiple scattering from the DS and from the material of the support structures for the DS. Because the geometry of these materials was complicated and difficult to model in simulations, the background from this source was approximated by fitting and connecting the regions on either side of the elastic-scattering peak in the DSPH histogram with a smooth function. We estimate the uncertainty in the yield caused by errors in the background approximation to be about $\pm 1.5\%$. Neutron-proton (*np*) scattering was used to check our estimation of the background uncertainty. For this purpose the DS was replaced with a hydrogenous scintillator, and a measurement of the relative differential cross section for *np* scattering was made. The measured cross section, as expected, was isotropic in the c.m. to within $\pm 2\%$, thereby confirming our error assessments.

Absolute neutron detection efficiency was determined by two methods. In the first method, the relative efficiency of each detector was measured by detecting neutrons emitted by the spontaneous fission of ^{252}Cf nuclei in a thin source located at the center of curvature of a hemispherical argon gas scintillator. The relative efficiencies (shape of the energy dependence) were measured to an accuracy of $\pm 1.5\%$. Efficiency measurements made with the ^{2}H(d,n)^{3}He reaction at discrete energies between 5.5 and 13.0 MeV were used to normalize the values obtained with the ^{252}Cf source to give absolute efficiencies between 0.25 and 13.0 MeV. The second method was done in collaboration with the Physikalisch-Technische Bundesanstalt (PTB) in Braunschweig, Germany. The absolute detection efficiency of two of our neutron detectors was determined from the measured light response function obtained at PTB for more than 30 neutron energies between 1 and 15 MeV. The efficiencies of these detectors were checked with those of previously calibrated PTB detectors. An uncertainty of $\pm 3\%$

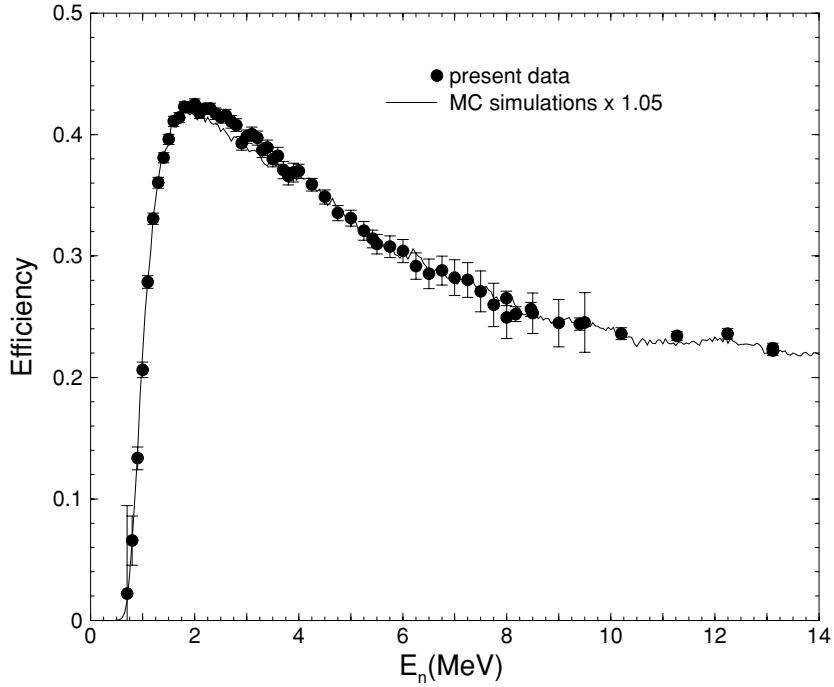

FIG. 5. Efficiency of one of the neutron detectors used in the present experiment as a function of neutron energy. The data are from measurements using neutrons from the ^{2}H$(d, n)^3$He reaction and from the spontaneous fission of ^{252}Cf. The error bars are for statistical uncertainties only. The curve is the prediction of an MC simulation done using the PTB code. The simulation is multiplied by a factor of 1.05 to fit the data.

was sufficient to account for differences in the results of the two methods, and this value was taken as the absolute uncertainty in the detector efficiencies. The efficiency for one of the detectors used in the measurements is shown in Fig. 5. The data are from the measurements made with the neutrons from the ^{2}H$(d,n)^3$He reaction and from the fission of ^{252}Cf. The curve is a simulation made using the code from the PTB group. The efficiency calculations for the different types of neutron detectors used in the present measurements were multipled by factors that ranged from 0.95 to 1.05 to fit the efficiency data. The scaled efficiency curves were used in the simulations of the experiment.

2. Determination of the DS light response function

The same elastic-scattering DSPH histograms used to determine the value of $\mathcal{L}$ were used to calibrate the light-output response function of the DS. The DS response function was determined from the centroids of the elastic-scattering peaks in the DSPH histograms. The channel of the recoil edge for *nd* elastic scattering to 180° was taken from the raw (with no neutron TOF constraint imposed in the software) DSPH histogram. The centroid channel for elastic scattering to each detector and the channel of the 180° recoil edge were plotted versus the recoil deuteron energy; see Fig. 6. The data were described using two functions. Below 5.6 MeV the points were fitted with a quadratic function of E, and above 5.6 MeV they were fitted with a linear function of E. The values and slopes of the functions were matched at 5.6-MeV deuteron energy. These functions were then used to calculate proton energies for the breakup data. Tornow *et al*. [47] verified that the light response of a deuterated scintillator to protons is related to the response to deuterons by

$$L_p(E) = \tfrac{1}{2} L_d(2E), \tag{3.2}$$

where $L_p(E)$ is the light output of a proton of energy E and similarly for L_d.

C. Breakup data analysis

A detector configuration was defined by the two neutron detectors involved in the triple coincidence with the DS. Each event for a particular configuration was identified as one of four types determined by the time correlation status of each neutron-detector signal relative to the signal from the DS. The time correlation status was either time correlated T_C or time uncorrelated T_U. The TOF spectrum of the T_U neutrons is flat and extends the full width of the coincidence window. The T_U neutron rate was determined from the part of the TOF spectrum with TOF values less than that of the prompt time-correlated γ rays. The T_C neutrons have TOF values covering the range between the elastic-scattering peak and threshold energy of the neutron detectors. Because T_U neutrons span the entire coincidence time window, any time slice will include some T_U neutrons.

The correlation status of each neutron was assigned using two time windows set in the TOF histogram of each detector in a configuration. The TOF histograms of the two detected neutrons in the configuration with $\theta_{n1} = \theta_{n2} = 50.5°$ and $\phi_{12} = 120°$ are shown in Fig. 7. The angles are the polar angles of the two neutrons and the azimuthal angle between their scattering planes. These histograms were collected with a pulse-height threshold set at one-half the Compton-scattering edge for γ rays from a ^{137}Cs source. In addition, events involving the detection of γ rays in either detector have been suppressed by pulse-shape analysis of the detector anode signals.

Four triple-coincidence event types were defined by the four possible combinations of two regions selected in the

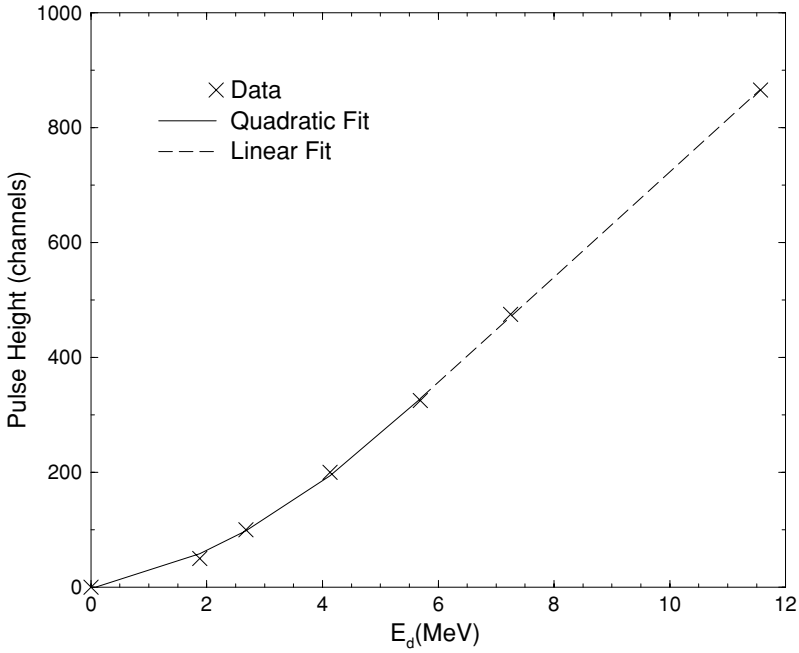

FIG. 6. Light response function of the deuterated scintillator (NE-232).

TOF spectra of the two neutron detectors: $(T_C + T_U)_1 \cdot (T_C + T_U)_2$, $(T_C + T_U)_1 \cdot T_{U2}$, $T_{U1} \cdot (T_C + T_U)_2$, and $T_{U1} \cdot T_{U2}$. An example of the two neutron TOF windows is shown in Fig. 7; the two sets of vertical lines define the regions where

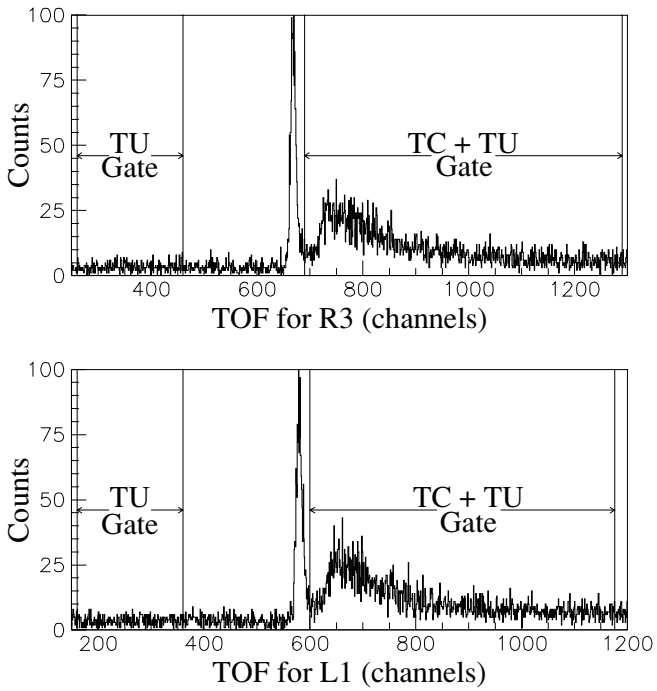

FIG. 7. Triple-coincidence TOF histograms for two neutron detectors and the DS used in the space-star configuration ($\theta_{n1} = \theta_{n2} = 50.5^\circ$, $\phi_{12} = 120^\circ$). These histograms contain only a fraction of the accumulated data. The regions in the spectra corresponding to events for which the signals in the DS and the neutron detector are time correlated and uncorrelated are indicated. (Here, *Tu* and *Tc* denote T_u and T_c; see text.)

the $T_C + T_U$ and T_U events fall. These event types shall be referred to as type-1, type-2, type-3, and type-4 events, respectively. The "$\cdot$" and "$+$" symbols are the logical AND and OR operators, and the subscripts denote the neutron detector number in the coincidence pair. Two histograms were accumulated for each event type, one of the total particle energy ($E_{\text{tot}} = E_{n1} + E_{n2} + E_p$) and a two-dimensional (2D) histogram of E_{n1} versus E_{n2}, the energies of the two neutrons. The energy of the proton E_p was determined from the DSPH using the measured light response function in Fig. 6 and Eq. (3.2). An example of a 2D histogram of E_{n1} vs. E_{n2} for type-1 events for the space-star configuration at $\theta_{n1} = \theta_{n2} = 50.5^\circ$ and $\phi_{12} = 120^\circ$ is shown in Fig. 8. This histogram was accumulated with the condition that only events that conserved total energy to within ± 2 MeV contributed. The curve is the point-geometry locus, which will be referred to as the *S* curve. The point geometry was defined by the center of the neutron production target, the center of the DS, and the center of each neutron detector.

The breakup events were taken as those in which the timing signals from both neutron detectors were correlated to the signal from the DS, i.e., those with $T_{C1} \cdot T_{C2}$ true. The type-1 events contain breakup events ($T_{C1} \cdot T_{C2}$) and accidental events ($T_{C1} \cdot T_{U2}$, $T_{U1} \cdot T_{C2}$, and $T_{U1} \cdot T_{U2}$). The yields for the accidental events were obtained by subtracting the yields for type-4 events from the sum of the yields for type-2 and type-3 events. The contribution of each accidental background type to the total energy spectrum is shown in Fig. 9 for the detector configuration at $\theta_{n1} = \theta_{n2} = 50.5^\circ$ and $\phi_{12} = 120^\circ$. Total energy plots of the seven configurations studied in the present work and listed in Table II are shown in Figs. 10 and 11. The fractional contribution of the accidental triple coincidences to the total number of triple-coincidence events was very configuration dependent and ranged from as low as 5% to as much as 20% (see Figs. 10 and 11). An example

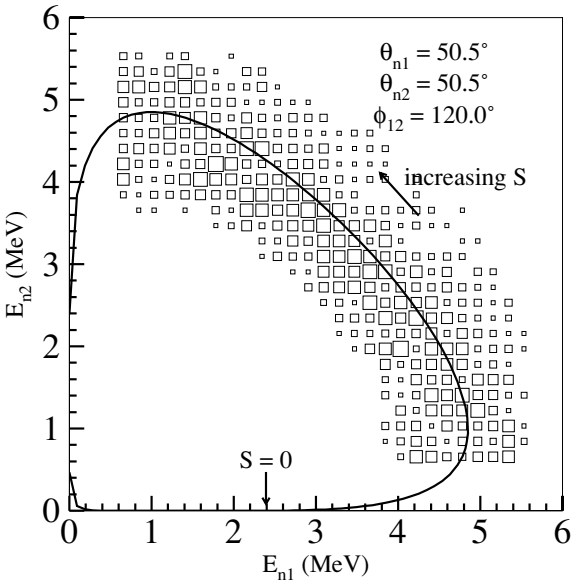

FIG. 8. Histogram of E_{n1} vs. E_{n2} for the space-star configuration. This histogram contains only a fraction of the accumulated data. The points are data, and the curve is the point-geometry kinematic locus.

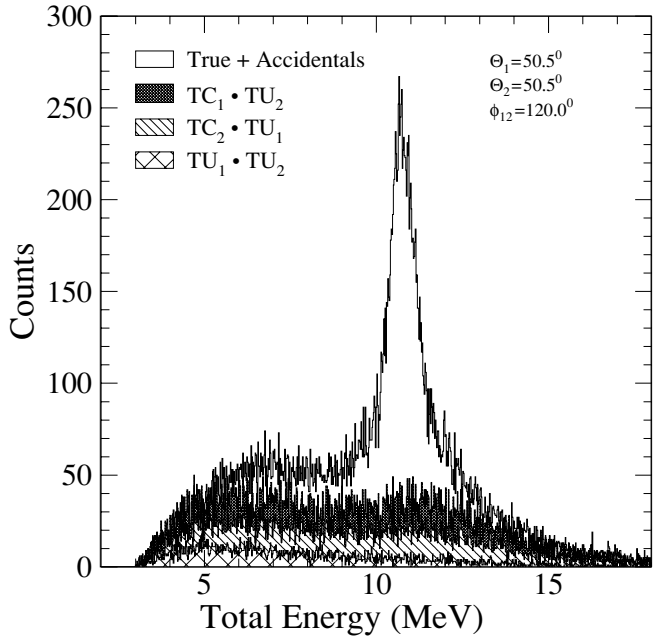

FIG. 9. Total energy histograms of type-1 events and of the three types of accidental events for the detector configuration. See text for details of the event types. (Here, *Tu* and *Tc* denote T_u and T_c; see text.)

of the yields projected into bins along the S curve is shown in Fig. 12.

The method used to determine the contribution of accidental-coincidence events was evaluated by accumulating a total energy histogram for a detector configuration ($\theta_{n1} = 62.5^\circ$, $\theta_{n2} = 50.5^\circ$, $\phi_{12} = 60^\circ$) that was kinematically forbidden with neutron-detector thresholds set at 1 MeV. In this case all counts in the histograms should have been due to accidental coincidences and multiple-scattering effects associated with kinematically allowed *nd* breakup events. The net yields (total − accidentals) in the total energy histogram were statistically consistent with zero.

The cross sections for each configuration were determined from the yields of breakup events along the S curve. Each event had to pass four requirements for the $E_{\rm tot}$ and E_{n1} vs. E_{n2} histograms to be incremented for that event. The requirements were (1) the pulse from each neutron detector must have an amplitude above the threshold value, (2) the amplitude of the pulse from the DS must be above the threshold value, (3) the pulse-shape times of each detector must fall within the range acceptable to be a neutron interaction in the detector, and (4) the total detected particle energy must be within the tolerance allowed by the experimental energy resolution. The detector threshold settings used in each configuration are listed in Table II. The thresholds were set relative to the Compton-scattering recoil edge for γ rays from a ^{137}Cs source. Such spectra were recorded every 48 hours to measure electronic drift of the detector pulse height. The events passing the above requirements were either from the breakup reaction or from accidental triple coincidences. In either case, the filtered events were used to increment histograms for each of the four event types.

TABLE II. Breakup configurations measured in the present work. Special kinematic points on the S curve are noted in the "special point" column. The "mirrored" column indicates whether two pairs of detectors were symmetrically arranged for the measurement. The neutron-detector thresholds are given relative to the Compton-scattering recoil edge for γ rays from a ^{137}Cs source. The threshold setting of the detector at θ_{n1} is given first.

θ_{n1}	θ_{n2}	ϕ_{12}	Special point	Mirrored	Threshold
50.5°	62.5°	180°	Collinear	yes	$\frac{1}{4}$, $\frac{1}{4}$
17.0°	50.5°	180°	Coplanar star	yes	$\frac{1}{2}$, $\frac{1}{4}$
50.5°	50.5°	120°	Space star	yes	$\frac{1}{4}$, $\frac{1}{4}$
39.0°	75.5°	180°	Collinear	no	$\frac{1}{4}$, $\frac{1}{4}$
39.0°	62.5°	180°	*np* FSI	no	$\frac{1}{4}$, $\frac{1}{4}$
32.0°	75.5°	180°	*np* FSI	no	$\frac{1}{4}$, $\frac{1}{4}$
17.0°	50.5°	120°	Near star	yes	$\frac{1}{4}$, $\frac{1}{4}$

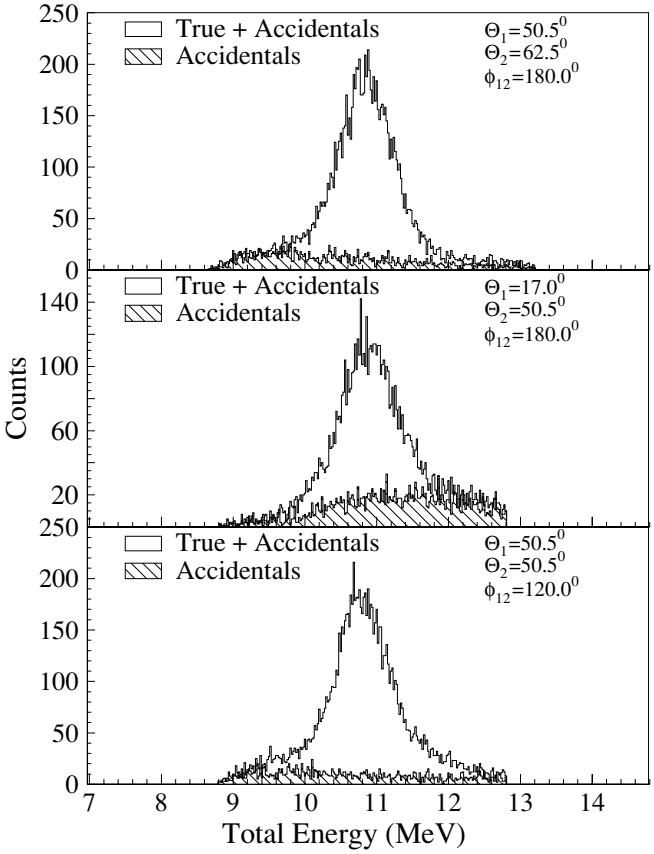

FIG. 10. Histograms of the total detected energy for the first three detector configurations in Table II. The contributions due to accidental triple coincidences are represented by the shaded areas. See text for details of the event types.

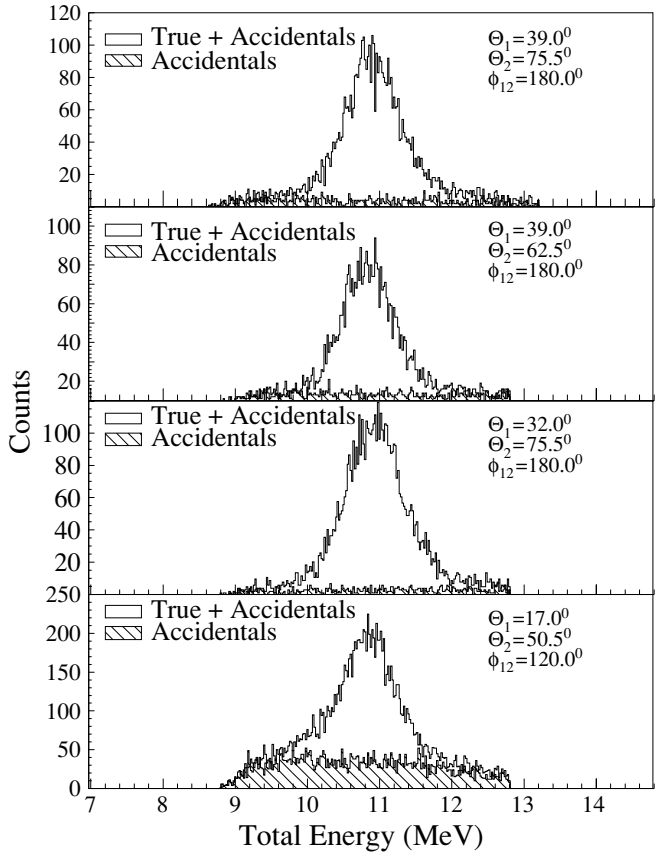

FIG. 11. Same as Fig.10, but for the last four detector configurations in Table II.

The yields for each event type were obtained by projecting the counts in the 2D histograms of E_{n1} vs. E_{n2} onto the S curve into 0.5-MeV-wide bins. The value of S was set to zero at the point where $E_{n2} = 0$ and increases with counterclockwise displacement along the S curve. The projection technique of Finckh *et al.* [23] was used. The particle energies (E_{n1}, E_{n2}, E_p) for each event were converted to momenta (k_{n1}, k_{n2}, k_p). Each momentum point was projected onto the nearest point on the point-scattering locus by minimizing the quantity

$$\left(k_{n1}^{\text{ideal}} - k_{n1}\right)^2 + \left(k_{n2}^{\text{ideal}} - k_{n2}\right)^2 + \left(k_p^{\text{ideal}} - k_p\right)^2. \qquad (3.3)$$

The superscript "ideal" refers to the point-scattering locus. After the projection, the data were then binned in 0.5-MeV steps along the S curve.

The cross section for each bin along the S curve was computed from the net breakup yields (total yields − accidental yields) for each detector configuration using the relationship

$$\frac{d^5\sigma(S)}{d\Omega_1 d\Omega_2 dS} = \frac{Y_{\text{bu}}(S)}{d\Omega_1\, d\Omega_2\, dS\, \bar{\alpha}(S)\, \bar{\epsilon}(S)\, \mathcal{L}}. \qquad (3.4)$$

$Y_{\text{bu}}(S)$ is the net breakup yields at S corrected for system dead times. $d\Omega_1$ and $d\Omega_2$ are the solid angles of the two neutron detectors. dS is the width of the energy bin along the S curve. $\bar{\epsilon}(S)$ is the energy-averaged value of the product of the two neutron detector efficiencies for the bin centered at S. $\bar{\alpha}(S)$ is the acceptance- and energy-averaged value of the product of the transmissions of the two emitted neutrons for the bin centered at S. $\mathcal{L}$ is the integrated target-beam luminosity.

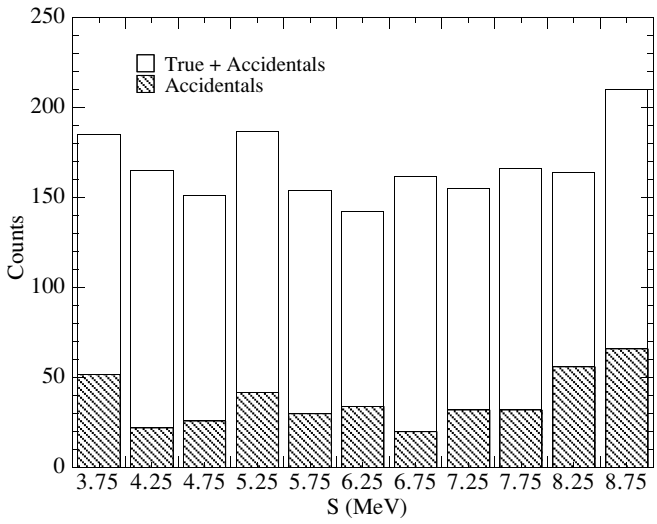

FIG. 12. True+accidental and accidental yields projected onto the locus for the configuration with $\theta_{n1} = \theta_{n2} = 50.5^\circ$, $\phi_{12} = 120^\circ$. Note: this plot contains only a fraction of the accumulated data.

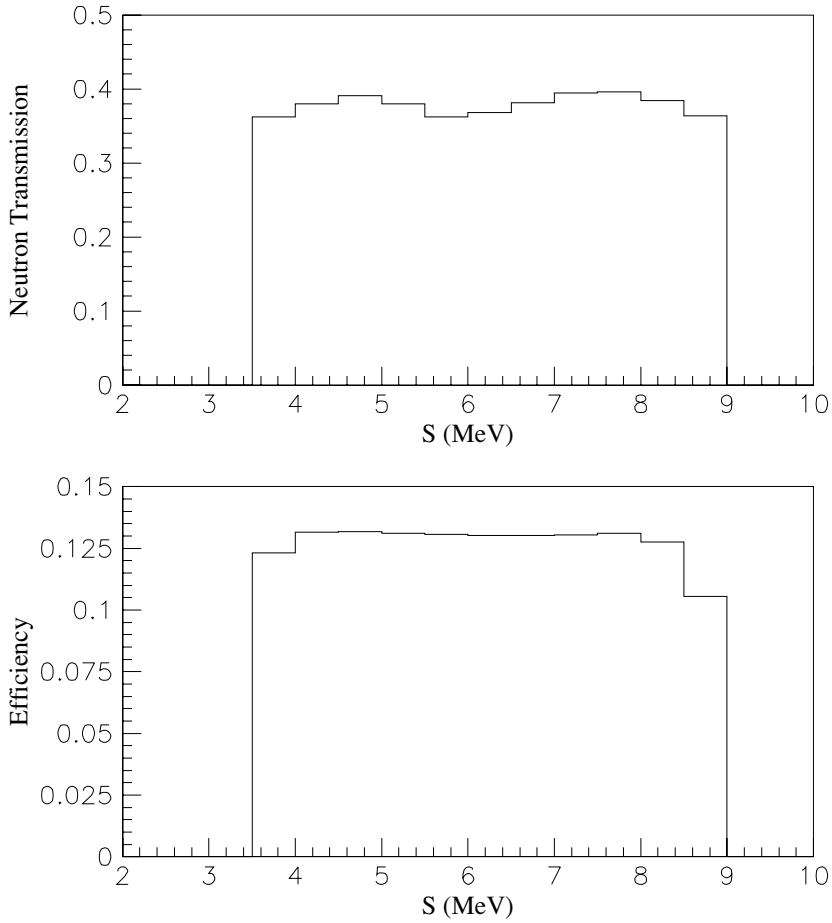

FIG. 13. Simulated mean values for the configuration with $\theta_{n1} = \theta_{n2} = 50.5^\circ$, $\phi_{12} = 120^\circ$. Top: Mean values of the product of the two neutron transmissions. Bottom: Mean values of the product of the two neutron detector efficiencies along the S curve.

The value of $\mathcal{L}$ was obtained from *nd* elastic scattering using the techniques described above. The values of $\epsilon(S)$ and $\alpha(S)$ were obtained from the computer simulations as described below.

The computer simulations were central to the determination of the breakup cross sections and to our interpretation of the experimental results. Only single scattering was modeled in the simulations of the breakup measurements. We studied the effects of multiple scattering on the breakup yields and found the contribution to be less than 3%. Because we correct for this effect, our reported breakup cross sections could be as much as 3% too high. We add $\pm 3\%$ to our systematic uncertainty to account for this effect. For each simulated locus of events, a point was randomly selected in each of the three detectors (the DS and the two neutron detectors). These points selected the neutron scattering angles; and with the incident neutron energy, they determined a kinematic locus. The energies of the three particles were calculated in 100-keV steps along the kinematic locus of E_{n1} vs. E_{n2} for the randomly chosen angles. The product of the two neutron transmissions and detector efficiencies were calculated for each point along the locus. However, these values were not necessarily identical to the ones determined in the experiment, because of the differences between the measured neutron energies and those calculated in the simulated events. The neutron energies in the experiment were determined from their measured TOF values and the mean flight-path lengths (center-to-center distance between the DS and the neutron detectors), while in the simulation the neutron energies were calculated from the kinematic equations. The neutron energies in the simulations were adjusted to match the experiment by computing the neutron velocity from the simulated TOF value and the mean flight-path length used with the experimental data. The simulated TOF value for each neutron was computed from the neutron energy and the distance between the points chosen in the DS and the neutron detector and then smeared with a Gaussian function of width equal to the time resolution of our system. The proton energy in the simulation was computed from the kinematic equations and then smeared with a Gaussian distribution of width equal to the energy resolution of the DS. The transmission factors and detector efficiencies were computed using the adjusted neutron energies for consistency with the treatment of the experimental data. The average over the angular acceptance and energy resolution of the experiment was computed for each bin along S. The typical value of $\bar{\alpha}$ for the breakup events was around 0.38 with an uncertainty of $\pm 1.3\%$. Examples of $\bar{\alpha}$ and $\bar{\epsilon}$ as a function of S are shown in Fig. 13 for the configuration with $\theta_{n1} = \theta_{n2} = 50.5^\circ$ and $\phi_{12} = 120^\circ$.

The statistical uncertainty in the breakup cross section was taken as the statistical uncertainty in Y_{bu} only. The statistical uncertainty in $\mathcal{L}$ was ignored because the elastic-scattering yields were measured to a statistical accuracy of better than 0.5%.

The systematic uncertainty in the breakup cross section is caused by the uncertainties in the luminosity, the neutron detection efficiencies, and the attenuation of the emitted neutrons in the material between the interaction sites in the DS and the neutron detector. Because our technique used *in situ* luminosity measurements that used the average efficiency of the detector array, our cross sections for the breakup reaction are effectively dependent on the absolute efficiency of only one of the two neutron detectors. The shape of the neutron detection efficiency curve as a function of energy was determined in an independent measurement to ±1.5%, as discussed in Sec. III B1. The uncertainty in the absolute neutron detector efficiency was estimated to be ±3% by comparing the results of two independent measurements (see Sec. III B1 for details). Because the $\mathcal{L}$ value includes the average of the detector efficiencies, the uncertainty calculation for the breakup cross section includes the uncertainty in the absolute efficiency of only one detector. The uncertainty in the calculated transmission of the scattered neutrons was ±1.3% and was mainly due to uncertainties in the neutron total cross sections used in the simulations for the scatterer constituents (carbon, deuterium, hydrogen, silicon, and oxygen). The sources of the uncertainties in $\mathcal{L}$ are described in Sec. III B1.

IV. RESULTS

Cross-section data for *nd* breakup were collected in 45 detector configurations using the experimental setup shown in Fig. 1. Here we report our data for the seven configurations in Table II. The detector angle pairs were chosen to measure the cross section for several special three-particle final-state configurations: the collinear, the coplanar star, the space star, and the *np* final-state interaction (FSI). The cross-section data for the seven detector configurations are compared in Figs. 14 and 15 to rigorous *nd* calculations made using the charge-dependent Bonn-B (CDBonn) *NN* potential [18]. The dashed and solid curves are point-scattering and finite-geometry calculations, respectively. Also shown in the figures (dotted curves) are point-scattering calculations using the CDBonn potential that include the Tucson-Melbourne (TM) 3NF [7]. The errors on the data in the figures are statistical only. The systematic uncertainty in the present data is ±6% (see Table III). The cross sections measured with mirrored detector pairs were consistent within statistical uncertainties. We report cross sections that include the finite-geometry effects of our experimental setup. No attempt was made to unfold finite-geometry effects from our measurements, since the procedure for reactions with three particles in the final state is arduous and often gives results with significant uncertainties. We chose the less cumbersome and much more accurate path of folding the finite geometry of our experiment into the theoretical predictions with MC simulations. The results are discussed below.

Our cross-section data for a collinear configuration is shown in Fig. 14(a) in comparison to the *nd* data of Strate *et al.* [21], the *pd* data of Rauprich *et al.* [30], and point-geometry and finite-geometry rigorous *nd* calculations. At the collinear point one particle is at rest in the c.m. and the other two travel along a line in opposite directions. For our detector arrangement,

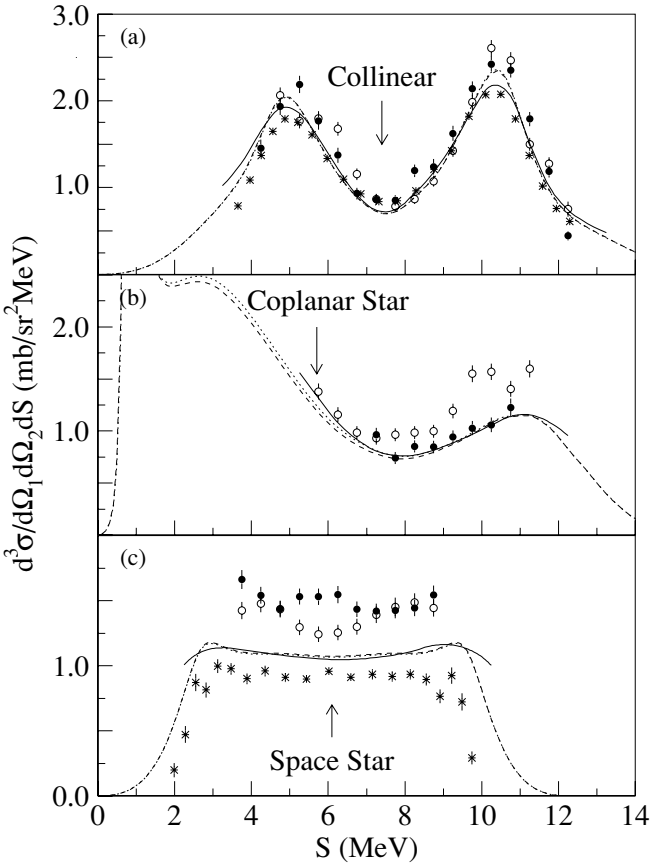

FIG. 14. Differential cross section for *nd* breakup at 13.0 MeV as a function of length along the point-geometry *S* curve for three detector configurations: (a) $\theta_{n1} = 50.5°$, $\theta_{n2} = 62.5°$, $\phi_{12} = 180°$, (b) $\theta_{n1} = 17.0°$, $\theta_{n2} = 50.5°$, $\phi_{12} = 180°$, and (c) $\theta_{n1} = 50.5°$, $\theta_{n2} = 50.5°$, $\phi_{12} = 120°$. The solid circles are the present data, the open circles are the *nd* data of Strate *et al.* [21], and the stars are the proton-deuteron data of Rauprich *et al.* [30]. The curves are predictions from rigorous *nd* calculations made with the charge-dependent Bonn-B *NN* potential [18]. The dashed and dotted curves are point-scattering calculations made without and with the TM 3NF [7] included, respectively. The solid curve is a simulation of the present experiment and includes the effects of finite geometry, detector energy resolution, and beam energy spread. It does not include three nucleon forces.

the proton is the particle at rest. The cross sections of Strate *et al.* and Rauprich *et al.* are for point scattering and should be compared to the dashed and dotted curves. Considering the size of finite-geometry effects (the difference between the solid and dashed curves) for this detector configuration, our data are in good agreement with those of Strate *et al.* However, both *nd* data sets are slightly higher than the theoretical predictions in the cross-section enhancements around 5 and 11 MeV on the *S* curve. These enhancements are in kinematic regions near *np* final-state interactions.

The data for the coplanar-star configuration are shown in Fig. 14(b). Our data are consistent with the theoretical predictions but lower than the data of Strate *et al.* by 10 to 25%. The cause of this discrepancy and others between the two *nd* data sets was identified by Setze *et al.* [31] as the differences in the treatment of backgrounds in the two

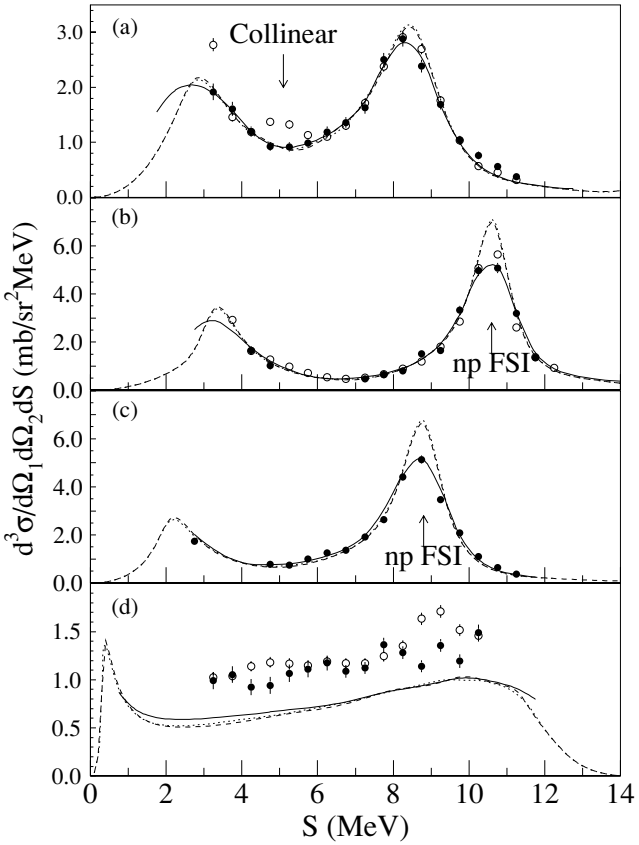

FIG. 15. Same as Fig. 14 except the angles are (a) $\theta_{n1} = 39.0^\circ, \theta_{n2} = 75.5^\circ, \phi_{12} = 180^\circ$, (b) $\theta_{n1} = 39.0^\circ, \theta_{n2} = 62.5^\circ, \phi_{12} = 180^\circ$, (c) $\theta_{n1} = 32.0^\circ, \theta_{n2} = 75.5^\circ, \phi_{12} = 180^\circ$, and (d) $\theta_{n1} = 17.0^\circ, \theta_{n2} = 50.5^\circ, \phi_{12} = 120^\circ$.

experiments. The backgrounds due to accidental coincidences were empirically determined in the present experiment from the neutron TOF spectrum (see Fig. 7). However, Strate *et al*. approximated their accidental-coincidence background by fitting a linear function to the tails of the peak in the total energy spectrum. As can be inferred from Figs. 10 and 11, the accuracy of the method employed by Strate *et al*. is incorrect, as the shape of the accidental background is clearly not always linear. For our setup, the backgrounds in the total energy spectra are nearly flat with the exception of the configuration at $\theta_{n1} = 17.0^\circ, \theta_{n2} = 50.5^\circ, \phi_{12} = 180^\circ$, which contains the coplanar-star point, and the one at $\theta_{n1} = 17.0^\circ, \theta_{n2} = 50.5^\circ, \phi_{12} = 120^\circ$. The backgrounds were high in these configurations relative to those in the other ones reported here. The high accidental-coincidence background in these configurations can be attributed to the high counting rate in the detectors at 17.0°.

TABLE III. Summary of systematic uncertainties.

Source	$\frac{\Delta\sigma}{\sigma} \times 100\%$
Shape of detector efficiency curve	±1.5
Absolute detector efficiency	±3.0
Neutron transmission	±1.3
Intergrated luminosity	±3.5
Breakup multiple scattering	±3.0
Total systematic uncertainty	±6.0

The data of Strate *et al*. for the space-star configuration are in good agreement with our data; see Fig. 14(c). However, both are about 20% higher than the theoretical predictions. Possible causes of this discrepancy between experiment and theory will be discussed in the next section.

Cross sections of the remaining four detector configurations are shown in Fig. 15. The agreement of our data with those of Strate *et al*. is generally good. However, a few exceptions should be noted. The cross-section enhancement at the collinear point in the data of Strate *et al*. is not present in our data; see Fig. 15(a). It was suggested that this deviation of the data from the theoretical prediction could be due to 3NF effects. Our data are contrary to this suggestion and agree well with predictions using only *NN* forces. In fact, when the TM 3NF is included in the present calculations, there is no enhancement at the collinear point due to 3NF effects. We suspect the enhancement in the cross-section data of Strate *et al*. at the collinear point is likely due to problems with their background subtraction method.

Our data for the configuration at $\theta_{n1} = 17.0^\circ$, $\theta_{n2} = 50.5^\circ$, $\phi_{12} = 120^\circ$ are slightly lower than the Strate *et al*. data. Again, this discrepancy is likely due to the background subtraction method they used. Both data sets are significantly higher than the theoretical predictions.

V. DISCUSSION

The good agreement between the predictions of rigorous *nd* calculations and data for a wide variety of observables over a broad energy range indicates that essential aspects of the interaction dynamics are treated properly in the calculations [10]. Discrepancies between calculations and data give hints of interactions or dynamics that are either neglected or incorrectly modeled. We investigate possible causes for the observed discrepancies between theory and the present data for two detector configurations.

The *np* FSI configurations are of particular interest because they provide a gauge for evaluating the accuracy of our data. In a final-state configuration where the relative momentum of two nucleons is near zero, the interaction among three nucleons is dominated by the pair of nucleons with low relative momentum. Under these conditions, the enhanced strength of the interaction between the two nucleons is expected to repress sensitivity to 3NF contributions. This intuition is supported by the present predictions made with the TM 3NF [4] in which the strength of the 3NF was adjusted to reproduce the experimental binding energy of the triton [48]. In all *np* FSI configurations measured in the present work, the predicted contribution to the cross section due to effects of this particular 3NF was less than 1%. Under these conditions, the theoretical calculations should accurately predict the cross sections. Because the cross sections for all configurations were measured simultaneously, the excellent agreement between our *np* FSI data and the *nd* calculations made with only *NN* forces (see Fig. 15) validates the accuracy of the normalization factor for our data set.

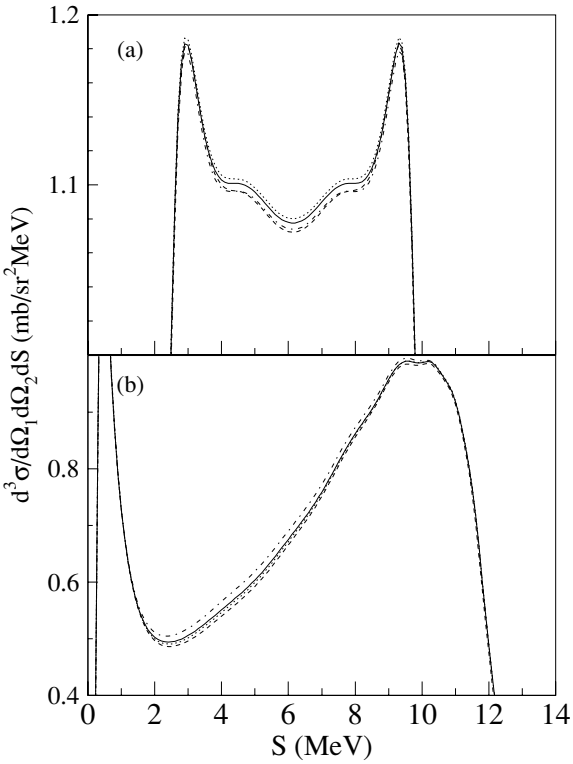

FIG. 16. Point-geometry cross-section calculations as a function of arclength along the ideal S curve for the configurations at (a) $\theta_{n1} = \theta_{n2} = 50.5^\circ$, $\phi_{12} = 120^\circ$, and (b) $\theta_{n1} = 17.0^\circ$, $\theta_{n2} = 50.5^\circ$, $\phi_{12} = 120^\circ$, for *nd* breakup at 13.0 MeV. The curves are rigorous calculations made with the Nijmegen-1 [16] (solid), Nijmegen-2 [16] (dotted), CD-Bonn [18] (dot-dashed), and AV18 [17] (dashed) *NN* potentials. Note that the vertical scale is offset from zero.

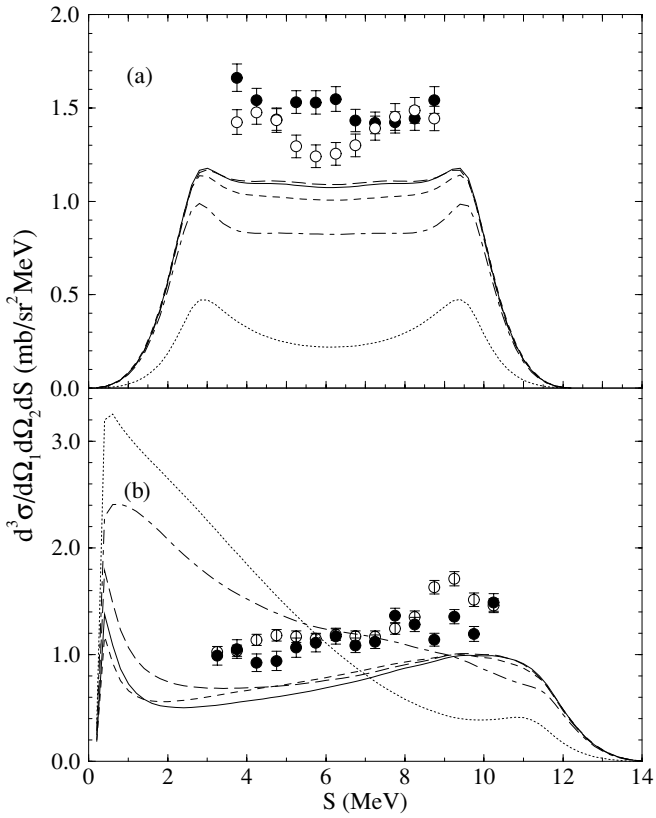

FIG. 17. Same as Fig. 16, but the curves are calculations made using the CD Bonn *NN* potential [18] with *NN* angular momentum states: $j \leqslant 3$ (solid), $^1S_0$ only (dotted), $^3S_1 - {}^3D_1$ only (dot-dashed) and $^1S_0 + {}^3S_1 - {}^3D_1$ (dashed). The short-dashed curve is a calculation made with the CD Bonn *NN* potential ($j \leqslant 3$) with the strength of the $^1S_0$ *nn* force decreased by 10%. The solid circles are the present *nd* data, and the open circles are the *nd* data of Strate *et al.* [21].

The discrepancy between theory and data for the space-star point is referred to as the *space-star anomaly* [31]. Our results for the configuration at $\theta_{n1} = 17.0^\circ$, $\theta_{n2} = 50.5^\circ$, $\phi_{12} = 120^\circ$ suggest that the anomaly is not limited to the space-star configuration but extends to other configurations. Of the seven configurations studied in this work, those with $\phi_{12} = 120^\circ$ were the only ones yielding data that significantly differed from the rigorous *nd* calculations. The cause of these discrepancies between data and theory are uncertain, but considerable circumstantial evidence points toward 3NF effects as being the culprit. We are led to this conclusion by considering each of the most plausible explanations for the discrepancy.

First, one posssibility is that the off-shell part of modern *NN* potentials is inconsistent with nature. The sensitivity of the cross section for the two discrepant configurations to the off-shell part of the *NN* interaction was studied by comparing calculations made with several phase-equivalent *NN* interactions. Because the off-shell behavior of the interactions differ substantially [19] and because the cross sections calculated using these realistic *NN* potentials have less than 2% dispersion (see Fig. 16), it is unlikely that reasonable changes in the off-shell structure of these potentials can significantly impact the space-star anomaly.

Second, there is the chance that deficiencies in the parametrization of the on-shell *NN* interaction might account for some of the discrepancy. As shown in Fig. 17, the cross section of both discrepant configurations is primarily due to the interference of the $^1S_0$ and $^3S_1 - {}^3D_1$ *NN* forces. The amplitudes interfere constructively in the space-star configuration and destructively in the other configuration. The difference in the signs of the interference terms for the two configurations further constrains the resolution of the discrepancies. The sensitivity of the cross sections to changes of the $^1S_0$ *nn* force was investigated by making calculations with the strength of the $^1S_0$ *nn* force in the CD Bonn potential multiplied by a factor of 0.9 (shown as the short-dashed curve in Fig. 17). The 10% reduction in the $^1S_0$ force strength reduces the *nd* integrated elastic and total cross section by 0.2% (which is well within the uncertainties in the data) and 2.3% (which is about one standard deviation below the data), respectively. Reducing the strength of the $^1S_0$ *nn* force gives contrary results for the two configurations. In the case of the space star, the calculated cross section is decreased by about 10%, thereby making the discrepancy between data and theory even greater. While for the other out-of-plane configuration, the calculated cross section is increased by about 10%, resulting in a slight reduction in the size of the discrepancy for this configuration. Because

the S-wave force components ($^1S_0$ and $^3S_1 - {}^3D_1$) are well determined from 2N data and tightly constrained by *nd* elastic scattering and total cross-section data, and because the P- and D-wave forces only play a minor role in the cross sections for these two configurations, the 20% difference between theory and data cannot be fully accounted for by deficiencies in the parametrization of these *NN* force components. Also, for the two configurations studied here, a change in the S-wave strength gives opposite effects in the calculated cross section. A change in the S-wave strength to reduce the size of the discrepancy for the space-star configuration worsens the discrepancy in the other configuration.

Third, effects due to relativistic kinematics on the phase-space factor have been shown to be small at low energies [24]. We estimate that these effects on the cross section are less than 1% at our energies. The good agreement between theory and our *np* FSI, collinear, and coplanar-star data supports these estimates.

Having made the claim that the observed discrepancies are likely to be due to 3NF effects, two questions arise. First, what could make these configurations more sensitive to 3NFs than the other five studied here? In particular, why should the space-star cross section be more sensitive to 3NFs than that of the coplanar star, which is the same exit-channel configuration rotated by 90° in the c.m.? And second, why are the predicted 3NF effects using the TM 3NF model an order of magnitude smaller than the observed difference between data and theory for these configurations and consistent with observations for the other five configurations?

The answer to the first question comes from considering the dynamics of the 3N reaction. The transition matrix evolves the initial system of a neutron and deuteron into the final state of three free nucleons. This means that each point on the kinematic locus of an angle configuration contains a unique set of matrix elements. Though the final states are similar for the coplanar and space stars, the momentum of the final-state particles in the two configurations are quite different, and consequently the configurations are formed by different sets of transition matrix elements. For this reason, each configuration should be examined autonomously with the condition that observables should vary smoothly with kinematically independent parameters. Two features distinguish the two discrepant configurations from the other five: (1) they are far from *NN* FSI and *NN* quasi-free-scattering (QFS) regions in phase space, and (2) the momentum vectors of the three final-state particles are not contained in a single plane.

Calculations made with the TM 3NF included are useful in examining the second question. They give the expected small effect from three-nucleon forces in kinematic regions near *NN* FSI and *NN* QFS. However, the effect of the inclusion of the TM 3NF is also small for the star and collinear configurations where the relative momenta between nucleons are about equal for the three pairs and where the momentum is transferred evenly among the particles. Note that in Figs. 14 and 15 it is difficult to distinguish dashed (without TM 3NF) from dotted (with TM 3NF) curves. In the case of the space star, the calculated change in the cross section due to the TM 3NF is in the opposite direction than that suggested by the data. The failure of the calculations with the TM 3NF to predict the measured cross sections means that either the data are incorrect or there is important physics missing from the calculations, or a combination of both. The consistency between the four cross-section measurements of the *nd* space star [21,31–33] strongly suggests that the data are correct within the reported uncertainties. The reported systematic uncertainties of ±5% in each data set leave some room for the latter possibility, i.e., both data and theory are slightly flawed. If discrepancies between data and calculations have their origin in deficiencies of the dynamical input in the calculations, then it most probably comes from 3NFs of quite different structure than the TM 3NF.

VI. CONCLUSION

In summary, we report new cross-section measurements for seven configurations in *nd* breakup at 13.0 MeV. Our data are binned in 0.5-MeV intervals along the S curve. Each data point has a statistical uncertainty of less than ±5%. The systematic uncertainty of the present data is ±5%. Our data are in agreement with those of Strate *et al*. [21] in four of six configurations. The two cases where the data disagree can be attributed to deficiencies in their background subtraction method.

Rigorous *nd* calculations using only 2N forces describe our data very well, except in two cases: the space-star configuration and the configuration at $\theta_{n1} = 17.0°$, $\theta_{n2} = 50.5°$, $\phi_{12} = 120°$. The *NN* FSI is of particular interest because in this configuration the interaction among the three nucleons is dominated by a single pair of nucleons, and therefore the contribution of the 3NF is expected to be relatively small. This fact is supported by the good agreement between theoretical calculations and our *np* FSI data. This agreement increases our confidence in the normalization procedure used in the present work and in our assigned systematic uncertainties.

Our data for the space-star configuration and the other out-of-plane configuration at $\theta_{n1} = 17.0°$, $\theta_{n2} = 50.5°$, $\phi_{12} = 120°$ are roughly 20% larger than the theoretical predictions based on modern *NN* interactions. By eliminating other possible explanations for these anomalously large discrepancies between theory and data, such as deficiencies in the parametrization of the on-shell 2N force, 2N off-shell effects, and relativistic kinematics effects, we are led to the conclusion that three-nucleon forces are important in these configurations. Two characteristics that distinguish these configurations from the other five are that the momentum vectors of the three final nucleons are not contained in the same plane and that they are far from the kinematic regions of *NN* final-state interactions and *NN* QFS. Because effects given by the TM 3NF are small for these configurations, the 3NF responsible for these discrepancies must have quite a different structure than the TM one. We strongly recommend more cross-section measurements for *nd* breakup in configurations where the momentum vectors are not contained in a single plane. Cross-section data for such configurations are important for resolving the space-star anomaly and for advancing our understanding of the role of three-nucleon forces in the low-energy continuum.

ACKNOWLEDGMENTS

This work was supported in part by the U.S. Department of Energy, Office of High Energy and Nuclear Physics, under Grant No. DE-FG05-91ER40619, by the Duke University Research Council, by the Deutsche Forschungsgemeinschaft Contract No. Me544/8-1, by the Croatian Ministry of Science Grant, by the European Community Contract No. CI1*-CT-91-0894, and by the Polish Committee for Scientific Research under Grant No. 2P03B02818. The calculations were performed on the Cray Y-MP of the North Carolina Supercomputing Center at Research Triangle Park, North Carolina, and on the Cray T90 and T3E of the NIC in Jülich, Germany.

[1] J. L. Friar and S. A. Coon, Phys. Rev. C **49**, 1272 (1994); J. L. Friar, D. Hüber, and U. van Kolck, *ibid*. **59**, 53 (1999), and references therein.
[2] Y. Wu, S. Ishikawa, and T. Sasakawa, Few-Body Syst. **15**, 145 (1993), and references therein.
[3] A. Nogga, H. Kamada, and W. Glöckle, Phys. Rev. Lett. **85**, 944 (2000).
[4] S. A. Coon and W. Glöckle, Phys. Rev. C **23**, 1790 (1981).
[5] P. U. Sauer, Prog. Part. Nucl. Phys. **16**, 35 (1986).
[6] R. G. Ellis, S. A. Coon, and B. H. J. McKellar, Nucl. Phys. **A438**, 631 (1985).
[7] S. A. Coon and M. T. Pena, Phys. Rev. C **48**, 2559 (1993).
[8] H. Witała, Th. Cornelius, and W. Glöckle, Few-Body Syst. **3**, 123 (1988).
[9] D. Hüber, H. Witała, and W. Glöckle, Few-Body Syst. **14**, 171 (1993).
[10] W. Glöckle, H. Witała, D. Hüber, and J. Golak, Phys. Rep. **274**, 107 (1996).
[11] M. M. Nagels, T. A. Rijken, and J. J. de Swart, Phys. Rev. D **17**, 768 (1978).
[12] M. Lacombe, B. Loiseau, J. M. Richard, R. Vinh Mau, J. Côté, P. Pirès, and R. de Tourreil, Phys. Rev. C **21**, 861 (1980).
[13] R. B. Wiringa, R. A. Smith, and T. L. Ainsworth, Phys. Rev. C **29**, 1207 (1984).
[14] R. Machleidt, K. Holinde, and Ch. Elster, Phys. Rep. **149**, 1 (1987).
[15] R. Machleidt, Advances in Nucl. Phys. **19**, 189 (1989).
[16] V. G. J. Stoks, R. A. M. Klomp, C. P. F. Terheggen, and J. J. de Swart, Phys. Rev. C **49**, 2950 (1994).
[17] R. B. Wiringa, V. G. J. Stoks, and R. Schiavilla, Phys. Rev. C **51**, 38 (1995).
[18] R. Machleidt, F. Sammarruca, and Y. Song, Phys. Rev. C **53**, R1483 (1996).
[19] R. Machleidt, Phys. Rev. C **63**, 024001 (2001).
[20] I. Šlaus, Y. Akaishi, and H. Tanaka, Phys. Rev. Lett. **48**, 993 (1982).
[21] J. Strate *et al*., Nucl. Phys. **A501**, 51 (1989).
[22] C. R. Howell *et al*., Phys. Rev. Lett. **61**, 1565 (1988).
[23] E. Finckh, K. Geissdörfer, R. Lin, S. Schindler, and J. Strate, Nucl. Instr. and Methods A **262**, 441 (1987).
[24] M. Allet *et al*., Phys. Rev. C **50**, 602 (1994).
[25] W. Glöckle, H. Kamada, H. Witala, D. Hüber, J. Golak, K. Miyagawa, and S. Ishikawa, Few-Body Syst. Suppl. **8**, 9 (1995).
[26] A. Picklesimer, R. A. Rice, and R. Brandenburg, Few-Body Syst. **19**, 47 (1995).
[27] J. Carlson, V. R. Pandharipande, and R. B. Wiringa, Nucl. Phys. **A401**, 59 (1983).
[28] J. E. McAninch, W. Haeberli, H. Witała, W. Glöckle, and J. Golak, Phys. Lett. **B307**, 13 (1993).
[29] M. Zadro *et al*., Nuovo Cimento **107A**, 185 (1994).
[30] G. Rauprich, S. Lemaitre, P. Niessen, K. R. Nyga, R. Reckenfelderbäumer, L. Sydow, and H. Paetz gen. Schieck, Nucl. Phys. **A535**, 313 (1991).
[31] H. R. Setze *et al*., Phys. Lett. **B388**, 229 (1996).
[32] M. Stephan *et al*., Phys. Rev. C **39**, 2133 (1989).
[33] K. Gebhardt, W. Jäger, C. Jeitner, M. Vitz, E. Finckh, T. N. Frank, Th. Januschke, W. Sandhas, and H. Haberzettl, Nucl. Phys. **A561**, 232 (1993).
[34] G. Nitzsche, Diploma thesis, University of Cologne, 1994.
[35] H. Patberg *et al*., Phys. Rev. C **53**, 1497 (1996).
[36] J. Zejma *et al*., Phys. Rev. C **55**, 42 (1997).
[37] H. Witała, D. Hüber, W. Glöckle, J. Golak, A. Stadler, and J. Adam, Jr., Phys. Rev. C **52**, 1254 (1995).
[38] H. Witała, D. Hüber, and W. Glöckle, Phys. Rev. C **49**, R14 (1994).
[39] C. R. Howell *et al*., Few-Body Syst. **2**, 19 (1987).
[40] Y. Tachikawa T. Yagita, M. Kondo, S. Minami, T. Ishida, K. Tsuruta, and K. Sagara, Nucl. Phys. **A684**, 583c (2001).
[41] A. Siepe, J. Deng, V. Huhn, L. Wützold, Ch. Weber, W. von Witsch, H. Witała, and W. Glöckle, Phys. Rev. C **65**, 0134010 (2002).
[42] H. Witała, W. Glöckle, D. Hüber, J. Golak, and H. Kamada, Phys. Rev. Lett. **81**, 1183 (1998).
[43] E. J. Stephenson, H. Witała, W. Glöckle, H. Kamada, and A. Nogga, Phys. Rev. C **60**, 061001 (1999).
[44] R. Bieber *et al*., Phys. Rev. Lett. **84**, 606 (2000).
[45] H. Sakai *et al*., Phys. Rev. Lett. **84**, 5288 (2000).
[46] R. V. Cadman *et al*., Phys. Rev. Lett. **86**, 967 (2001).
[47] W. Tornow, W. Arnold, J. Herdtweck, and G. Mertens, Nucl. Instr. and Methods A **244**, 477 (1986).
[48] A. Nogga, D. Hüber, H. Kamada, and W. Glöckle, Phys. Lett. **B409**, 19 (1997).